



Cu₂(OH)₂CO₃ clusters: Novel noble-metal-free cocatalysts for efficient photocatalytic hydrogen production from water splitting

Zhikang He^a, Junwei Fu^a, Bei Cheng^a, Jiaguo Yu^{a,b,*}, Shaowen Cao^{a, **}

^a State Key Laboratory of Advanced Technology for Materials Synthesis and Processing, Wuhan University of Technology, Wuhan 430070, PR China

^b Department of Physics, Faculty of Science, King Abdulaziz University, Jeddah 21589, Saudi Arabia

ARTICLE INFO

Article history:

Received 30 October 2016

Received in revised form 5 December 2016

Accepted 8 December 2016

Available online 9 December 2016

Keywords:

Photocatalysis

Hydrogen production

Noble-metal-free cocatalyst

ABSTRACT

Photocatalytic hydrogen evolution is a potential route for converting inexhaustible solar energy into available clean chemical energy. Herein, highly efficient and stable Cu₂(OH)₂CO₃/TiO₂ photocatalysts for hydrogen generation are prepared by incorporating Cu₂(OH)₂CO₃ clusters onto the surface of TiO₂ through a facile precipitation method. The obtained Cu₂(OH)₂CO₃/TiO₂ photocatalyst with optimal Cu₂(OH)₂CO₃ content of 0.5 mol% shows an outstanding photocatalytic H₂-production rate of 6713 μmol h⁻¹ g⁻¹ (with apparent quantum efficiency of 15.4% at 365 nm), which is comparable to the excellent Pt/TiO₂ photocatalyst and more efficient than other copper species modified TiO₂ photocatalyst. The formation of Cu₂(OH)₂CO₃/Cu⁺/Cu⁰ clusters essentially contribute to the enhanced H₂-production activity by reducing the over-potential of water reduction and promoting the transfer of photogenerated electrons from the conduction band of TiO₂ to the Cu₂(OH)₂CO₃/Cu⁺/Cu⁰ clusters. A high stability of the Cu₂(OH)₂CO₃/TiO₂ photocatalyst is achieved due to the re-oxidation process of Cu⁺/Cu⁰ to Cu₂(OH)₂CO₃ and structure confinement of Cu₂(OH)₂CO₃ clusters in the mesopores of TiO₂. This work brings in new insight in developing low-cost noble-metal-free photocatalytic system for solar-to-fuel conversion.

© 2016 Elsevier B.V. All rights reserved.

1. Introduction

Converting inexhaustible solar energy into clean hydrogen energy is a promising route to satisfy the sustainable development of human society [1–7]. Since the pioneering work of photocatalytic water splitting on TiO₂ electrodes reported by Honda and Fujishima in 1972 [8], photocatalytic hydrogen generation has been demonstrated to be a potential strategy in such solar-to-hydrogen conversion [9–11]. TiO₂ has been widely used in the photocatalytic hydrogen evolution reaction due to its abundance, non-toxicity, as well as high chemical and thermal stability [12–15]. However, the photocatalytic hydrogen production efficiency over bare TiO₂ remains limited, mainly because of its wide band gap and rapid recombination of photogenerated electron–hole pairs [16–19]. Many efforts have been devoted to solving these problems and improving the solar-to-hydrogen conversion efficiency, such

as loading of noble metals [20,21], sensitizing by inorganic complexes or organic dyes [22,23], doping with metal cations [24–26] or nonmetal elements [27,28], coupling with other semiconductors [29,30], and so on. In particular, deposition of noble metals such as Pt, Au and Pd can significantly promote the photocatalytic hydrogen production of TiO₂ [31–34]. This is because the deposited noble metals can act as electron sinks to efficiently separate the photogenerated electron–hole pairs [22,35]. Moreover, these noble metals can lower the over-potential of proton reduction to boost the reaction process [3,36]. However, noble metals are rare and too expensive. The development of highly active but low-cost cocatalysts as substitutes of noble metals is of great significance for photocatalytic hydrogen production, although it is still challenging.

Recently, Cu-containing species have shown excellent ability to enhance the photocatalytic hydrogen production performance of TiO₂ [37–45]. For instance, Li et al. [46] prepared Cu₂O/TiO₂ composite photocatalyst with significantly improved performance of photocatalytic hydrogen evolution, which was attributed to the close contact between Cu₂O and TiO₂ improving the interfacial charge transfer and suppressing the charge recombination. Xiao et al. [47] employed low-cost metallic copper nanowires as a substitute for noble metals to couple with TiO₂, and found the formation of Schottky barrier on the Cu/TiO₂ interface facilitated the photoelectron transfer, thus resulting in enhanced photocatalytic

* Corresponding author at: State Key Laboratory of Advanced Technology for Materials Synthesis and Processing, Wuhan University of Technology, Wuhan 430070, PR China.

** Corresponding author.

E-mail addresses: jiaguoyu@yahoo.com, yujiagu093@163.com (J. Yu), swcao@whut.edu.cn (S. Cao).

hydrogen generation. Other Cu-containing species (such as CuO and Cu(OH)₂) modified TiO₂ were also reported [48,49] with enhanced photocatalytic hydrogen production activity as compared to bare TiO₂. The corresponding functional component was usually Cu₂O or Cu derived from the photo-reduction of the copper species. In comparison with these reported Cu-containing species, Cu₂(OH)₂CO₃ as a common copper-based compound possesses a greater solubility product constant, which suggests that Cu₂(OH)₂CO₃ can easily release more free Cu²⁺ in aqueous solution. The resultant free Cu²⁺ in aqueous solution can be reduced into Cu⁺/Cu⁰ by the photo-generated electrons of TiO₂ [50–52]. Consequently, more effective component Cu⁺/Cu⁰ can be obtained from Cu₂(OH)₂CO₃ during the photocatalytic process, which essentially promote the photocatalytic hydrogen evolution over Cu₂(OH)₂CO₃/TiO₂ photocatalyst. Moreover, it is expected that the Cu⁺/Cu⁰ component can be re-oxidized into Cu₂(OH)₂CO₃ after photocatalytic reaction, which enables a good stability of the Cu₂(OH)₂CO₃/TiO₂ photocatalyst.

Herein, we incorporate Cu₂(OH)₂CO₃ clusters onto the surface of TiO₂ (P25) through a facile precipitation method. The resultant Cu₂(OH)₂CO₃/TiO₂ photocatalyst shows a stable and comparable photocatalytic H₂-production activity to that of Pt/TiO₂ photocatalyst, with apparent quantum efficiency of 15.4% at 365 nm. It is also demonstrated that Cu₂(OH)₂CO₃ clusters are more efficient than other copper species, as a substitute for noble metal cocatalyst in the photocatalytic hydrogen evolution reaction.

2. Experimental

2.1. Sample preparation

TiO₂ (P25, 20% rutile and 80% anatase) powder was purchased from Degussa Co., Ltd., Germany. Copper nitrate (Cu(NO₃)₂), sodium carbonate (Na₂CO₃) and sodium hydrate (NaOH) were supplied by Sinopharm Chemical Reagent Co., Ltd., China. All the chemical reagents were of analytical grade and used without further purification.

Cu₂(OH)₂CO₃/TiO₂ photocatalysts were prepared by a precipitation method. Typically, 0.5 g of P25 was dispersed in 50 mL of Na₂CO₃ aqueous solution, and then 10 mL of Cu(NO₃)₂ aqueous solution was added dropwise under vigorous stirring. The molar ratio of Na₂CO₃ to Cu(NO₃)₂ in the suspension was 3:2. A certain amount of 0.25 M NaOH aqueous solution was added to promise a basic (pH = 8) environment. The obtained suspension was kept stirring for 6 h at room temperature. Then the resulting precipitates were collected and washed thoroughly with distilled water and ethanol for several times. Finally, the as-prepared products were dried at 80 °C for 10 h. The nominal molar ratios (R) of Cu to TiO₂ were designed as 0, 0.1, 0.25, 0.5, 1 and 4 mol% (see Table 1), and the obtained samples were labeled as C0, C0.1, C0.25, C0.5, C1 and C4, respectively. For comparison, pure Cu₂(OH)₂CO₃ was also prepared under the same experimental conditions without the addition of P25, and was labeled as C100. In addition, different Cu-containing species modified TiO₂ photocatalysts (Cu/P25, Cu₂O/P25, CuO/P25 and Cu(OH)₂/P25) and Pt modified TiO₂ (Pt/P25) were prepared with 0.5 mol% Cu or Pt loading content (see experimental details in Supporting information).

2.2. Characterization

X-ray diffraction (XRD) patterns were recorded on an X-ray diffractometer (Rigaku, Japan) with Cu-K α radiation ($\lambda = 1.5406 \text{ \AA}$) and a scan rate (2θ) of $0.05^\circ \text{ s}^{-1}$ at the angle range of $10\text{--}80^\circ$. Transmission electron microscopy (TEM) and high-resolution transmission electron microscopy (HRTEM) images were obtained from a JEM-2100F electron microscope (JEOL, Japan), with an

accelerating voltage of 200 kV. UV-vis diffuse reflectance spectra (UV-vis DRS) of the samples were measured on a UV-vis spectrophotometer (UV2550, Shimadzu, Japan) over the range of 250–800 nm using BaSO₄ as a reference. Photoluminescence (PL) spectra were recorded at room temperature using a fluorescence spectrophotometer (F-7000, Hitachi, Japan). The excitation wavelength was 325 nm, and the width of excitation and emission slits were both 5.0 nm. X-ray photoelectron spectra (XPS) were recorded on an ESCALab 250Xi (Thermo Fisher) equipped with monochromatic 150 W Al-K α radiation. The binding energy was calibrated with reference to the C1 s peak at 284.8 eV. Nitrogen adsorption–desorption isotherms were measured on a Tristar II 3020 (Micromeritics Instruments, USA) nitrogen adsorption apparatus. All samples were degassed at 100 °C under vacuum for 4 h. The adsorption data in the relative pressure (p/p_0) range of 0.05–0.3 were used to determine the specific surface area according to the BET (Brunauer–Emmett–Teller) method. The Barret–Joyner–Halender (BJH) method was applied to calculate the pore size distribution. The pore volume and average pore size were determined based on the adsorbed nitrogen volume at the relative pressure (p/p_0) of 0.99. The inductively coupled plasma atomic emission spectrometry (ICP-AES) was recorded on an Optima 4300 DV spectrometer (Perkin Elmer).

2.3. Photoelectrochemical measurements

The transient photocurrent response was measured by an electrochemical analyzer (CHI 760E Instruments) in a standard three-electrode system, using the as-prepared samples as the working electrode with an active area of *ca.* 1.0 cm², a Pt wire as the counter electrode and Ag/AgCl (saturating KCl) as the reference electrode, respectively. Bias potentials applied on the working electrode were 0.5 V. A low power UV-LED (3 W, 365 nm) was utilized as the light source. The working electrode was immersed into 0.5 M Na₂SO₄ aqueous solution. The electrochemical impedance spectroscopy (EIS) and the cyclic voltammetry (CV) were also measured in the above-mentioned three-electrode system. The EIS was performed by applying the bias of the open circuit voltage (VOC) and recorded over a frequency range of 0.05–10⁵ Hz with an ac amplitude of 10 mV. The CV curve was recorded at a scan rate of 0.1 V s^{-1} between 0.01 and 1.61 V (vs. RHE), and the initial scan polarity is negative.

Linear scan voltammogram (LSV) measurement was performed in 1 M KOH solution without the light irradiation, using glassy carbon (GC) electrodes with a diameter of 3 mm. Samples (5 mg) were dispersed in mixed solvent of deionized water (1 mL), 2-propanol (0.25 mL) and Nafion solution (10 mL) *via* sonication for more than 1 h. The suspension (3 mL) was then drop-casted on GC electrodes, and the solvent was allowed to be evaporated at 80 °C for around 10 min. Potentials were referenced to reversible hydrogen electrode (RHE) by $E_{\text{RHE}} = E_{\text{Ag/AgCl}} + 0.197 + 0.059 \times \text{pH}$. The scan rate of the linear scan voltammogram is 10 mV s^{-1} .

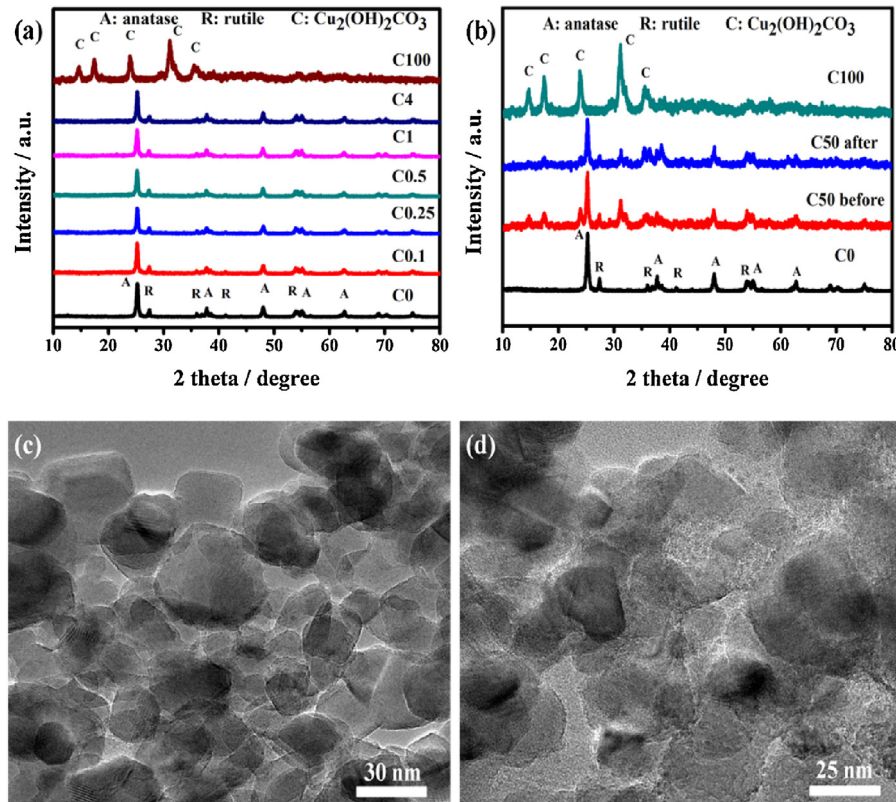
2.4. Photocatalytic H₂-production tests

The photocatalytic hydrogen generation experiments were carried out in a 100 mL three-necked Pyrex glass reactor with a 300 W Xenon lamp (Changzhou Siyu Science Co., Ltd., China) as the UV-vis light source. In a typical experiment, 50 mg of the as-prepared photocatalyst was added into 80 mL of aqueous methanol solution (25 vol%). The suspension was put into an ultrasonic bath for 5 min and then N₂ gas was purged throughout the reactor for 30 min to completely remove the dissolved oxygen. Then the sealed reactor was irradiated under the Xenon arc lamp for 1 h. After irradiation, 0.4 mL gas product was sampled through the septum. The evolved hydrogen was analyzed by gas chromatograph (GC-14C, Shimadzu,

Table 1

Cu species contents and physical properties for various samples.

Samples	R (mol%)	$\text{Cu}_2(\text{OH})_2\text{CO}_3$ (mol%)(ICP-AES)	S_{BET} ($\text{m}^2 \text{g}^{-1}$)	V_{Pore} ($\text{cm}^3 \text{g}^{-1}$)	Average pore size (nm)
C0	0	–	47	0.16	13.4
C0.1	0.1	0.023	45	0.30	27.2
C0.25	0.25	0.135	45	0.31	28.0
C0.5	0.5	0.286	45	0.31	28.0
C1	1	0.525	45	0.31	27.4
C4	4	3.37	41	0.27	26.0

**Fig. 1.** (a) XRD patterns of the C0, C0.1, C0.25, C0.5, C1, C4 and C100 samples; (b) XRD patterns of the C0, C50 before and after irradiation, C100 samples; TEM images of samples C0 (c) and C0.5 (d).

Japan, and 5 Å molecular sieve column) with a thermal conductivity detector (TCD) using N_2 as the carrier gas.

The apparent quantum efficiency (QE) was measured under the similar photocatalytic reaction conditions. Four low-power UV-LEDs (3 W, 365 nm) (Shenzhen LAMPLIC Science Co., Ltd., China) located 1 cm away from the reactor in four different directions were used as light sources to drive the photocatalytic reaction. The illuminated areas and focused intensity on the flask for each UV-LED were 1 cm^2 and *ca.* 110 mW/cm², respectively. The QE was measured and calculated according to Eq. (1):

$$\text{QE}(\%) = \frac{\text{number of reacted electrons}}{\text{number of incident photons}} \times 100 \quad (1)$$

$$= \frac{\text{number of evolved H}_2 \text{ molecules} \times 2}{\text{number of incident photons}} \times 100$$

3. Results and discussion

3.1. Phase structure and morphology

The phase structures and average crystallite sizes of the as-prepared samples were investigated by XRD analysis. Fig. 1a shows

the XRD patterns of the $\text{Cu}_2(\text{OH})_2\text{CO}_3/\text{TiO}_2$ photocatalysts with various $\text{Cu}_2(\text{OH})_2\text{CO}_3$ contents. It can be found that only the phase of anatase and rutile can be detected in C0, C0.1, C0.25, C0.5, C1 and C4 samples, and no characteristic diffraction peaks of $\text{Cu}_2(\text{OH})_2\text{CO}_3$ were observed. This is due to the low loading content and good dispersion of $\text{Cu}_2(\text{OH})_2\text{CO}_3$ clusters [49]. For sample C100, the typical diffraction peaks at $2\theta = 14.8^\circ, 17.6^\circ, 24.1^\circ, 31.2^\circ$ and 35.6° can be indexed to the (020), (120), (220), (201) and (240) planes of $\text{Cu}_2(\text{OH})_2\text{CO}_3$ (PDF No. 41-1390), respectively. To further confirm the phase structure of $\text{Cu}_2(\text{OH})_2\text{CO}_3$ in the $\text{Cu}_2(\text{OH})_2\text{CO}_3/\text{TiO}_2$ composite samples, the sample C50 with nominal molar ratio of 50 mol% of Cu to TiO_2 was synthesized and the main XRD diffraction peaks of $\text{Cu}_2(\text{OH})_2\text{CO}_3$ can be distinguished in Fig. 1b. These main peaks of $\text{Cu}_2(\text{OH})_2\text{CO}_3$ can be still observed after irradiation, indicating the good stability of $\text{Cu}_2(\text{OH})_2\text{CO}_3$ for photocatalytic application. The microstructures of the samples were examined by TEM observation. It can be found that smooth surfaces are obtained for pure TiO_2 particles (Fig. 1c), while numerous ultra-small dots sized in *ca.* 1–3 nm can be evidenced after the loading of $\text{Cu}_2(\text{OH})_2\text{CO}_3$ (Fig. 1d). The result indicates that $\text{Cu}_2(\text{OH})_2\text{CO}_3$ clusters are uniformly dispersed on the surfaces of TiO_2 , which can provide more photocatalytic active sites.

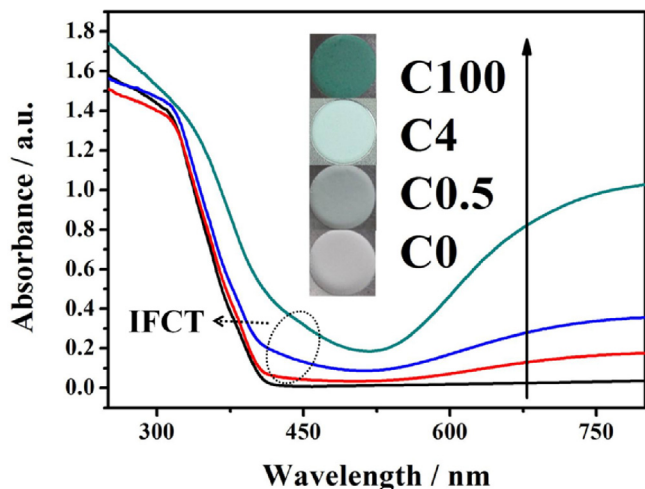


Fig. 2. UV-vis diffuse reflectance spectra and the corresponding optical photographs (inset) of the samples C0, C0.5, C4 and C100.

3.2. UV-vis diffuse reflectance spectra

Optical absorption properties can greatly affect the photocatalytic activity of semiconductors. In this case, UV-vis DRS were carried out to study the optical absorption properties of the typical samples, as shown in Fig. 2. For the pure TiO_2 (C0), the intrinsic band gap absorption of rutile TiO_2 sharply increases from 410 nm, corresponding to the band gap of 3.0 eV [53]. After the loading of $\text{Cu}_2(\text{OH})_2\text{CO}_3$ clusters, the absorption intensities at 410–500 nm and 700–800 nm are significantly enhanced. With increasing the $\text{Cu}_2(\text{OH})_2\text{CO}_3$ content, the prepared samples show gradually increased absorption, which is in agreement with the color change from white to green (inset in Fig. 2). Particularly, the absorption band located at 700–800 nm can be ascribed to the d–d transition of Cu(II), and the absorption band approximately at 410–500 nm can be attributed to the direct interfacial charge transfer (IFCT) from the valence band (VB) of TiO_2 to Cu^{2+} [54,55], implying the successful incorporation of Cu^{2+} species on the surface of TiO_2 . Such IFCT-induced light harvesting can also help to generate more photoinduced electron–hole pairs, for a better photocatalytic activity.

3.3. BET surface areas and pore size distributions

The nitrogen adsorption–desorption measurements were carried out to determine the specific surface area and porosity property of the samples, which are important factors to affect photocatalytic reactions. The nitrogen adsorption–desorption isotherms and corresponding pore size distribution curves of the samples C0, C0.5 and C4 are displayed in Fig. 3. All samples have similar nitrogen adsorption–desorption isotherms of type IV, on the basis of the IUPAC classification [56]. Hysteresis loops formed at high relative pressure range indicate the formation of large mesopores and macropores. The shapes of the hysteresis loops are of type H3, which is associated with slit-like pores [57]. The pore size distribution curves (inset in Fig. 3) show a wide range of 2–100 nm, confirming the existence of mesopores and macropores. Further observation shows that the curve of the pure TiO_2 (C0) has two peaks at pore diameters of ca. 2.5 and 50 nm, while the peak at ca. 2.5 nm disappears in the curves of $\text{Cu}_2(\text{OH})_2\text{CO}_3/\text{TiO}_2$ samples (C0.5 and C4). It is known from TEM observation that the $\text{Cu}_2(\text{OH})_2\text{CO}_3$ clusters are sized in 1–3 nm, which can fill in those mesopores of ca. 2.5 nm and result in larger average pore size of $\text{Cu}_2(\text{OH})_2\text{CO}_3/\text{TiO}_2$ samples. Quantitative details of the BET specific surface area, pore

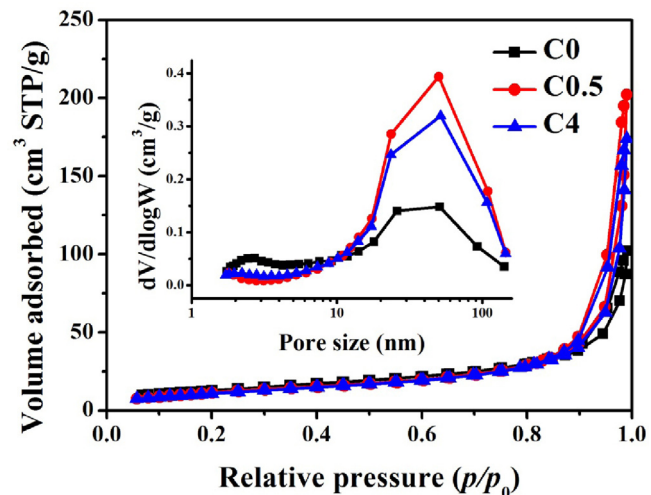


Fig. 3. Nitrogen adsorption–desorption isotherms and the corresponding pore-size distribution curves (inset) of the samples C0, C0.5 and C4.

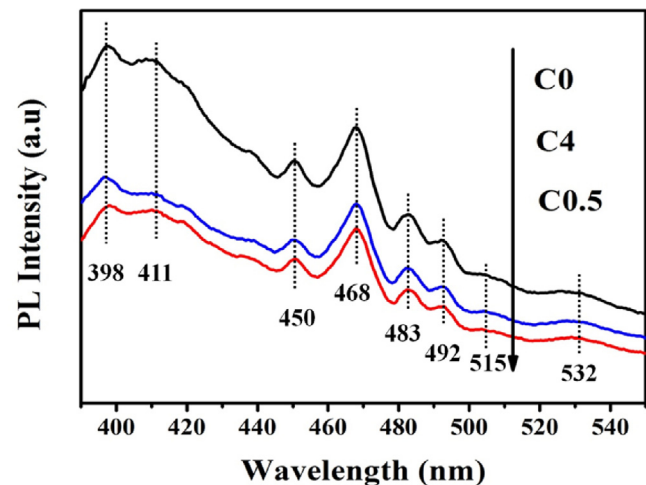


Fig. 4. Comparison of the PL spectra of the samples C0, C0.5 and C4.

volume and average pore size are listed in Table 1. It can be seen that no obvious change is observed for the specific surface areas after the loading of $\text{Cu}_2(\text{OH})_2\text{CO}_3$ clusters. However, in comparison with the pure TiO_2 sample, the $\text{Cu}_2(\text{OH})_2\text{CO}_3/\text{TiO}_2$ samples possess distinctly increased average pore sizes and pore volumes, which can facilitate the exposure of active sites and promote the photocatalytic efficiency.

3.4. PL spectra

PL spectra were employed to estimate the recombination of photogenerated electron–hole pairs of photocatalysts, as the intrinsic PL emission arises from the recombination of free charge carriers [58]. Similar shapes are observed for the PL spectra of the samples C0, C0.5 and C4 (Fig. 4), with four main emission peaks at 398, 411, 450 and 468 nm, respectively. In particular, the two major peaks at 398 and 411 nm are assigned to the interband PL phenomenon with the photo-energy approximately equal to the band gaps of anatase and rutile, respectively [49]. And the emission peaks at 450 and 468 nm are ascribed to band edge free excitons [49]. And the rest four small peaks in the wavelength range of 480–550 nm originate from excitonic PL, which mainly result from surface defects or oxygen vacancies [59]. Obviously, the PL intensities for the

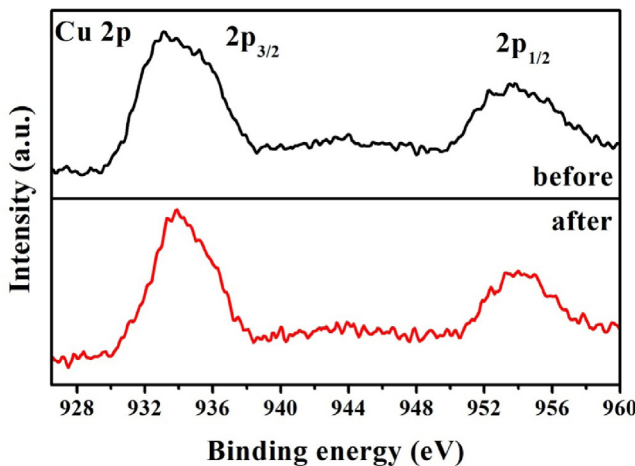


Fig. 5. High-resolution XPS spectra of Cu 2p of the C0.5 sample before and after photocatalytic reaction.

samples C0.5 and C4 are much lower than that of sample C0. This suggests that the recombination of photogenerated electron–hole pairs in the $\text{Cu}_2(\text{OH})_2\text{CO}_3/\text{TiO}_2$ samples is successfully suppressed, because the photogenerated electrons can transfer from the conduction band (CB) of TiO_2 to $\text{Cu}_2(\text{OH})_2\text{CO}_3$ clusters. Such decreased recombination rate of electrons and holes is of great importance to promote the photocatalytic reaction. Note that the sample C0.5 has the lowest PL intensity, indicates that an optimal loading content of $\text{Cu}_2(\text{OH})_2\text{CO}_3$ is important, since excess $\text{Cu}_2(\text{OH})_2\text{CO}_3$ clusters can adversely work as recombination centers [60].

3.5. XPS analysis

XPS analysis was performed to further characterize the chemical state of copper in the $\text{Cu}_2(\text{OH})_2\text{CO}_3/\text{TiO}_2$ photocatalyst. Fig. 5 shows the comparison of Cu 2p high-resolution XPS spectra of C0.5 before and after photocatalytic reaction. The binding energies (Cu^{2+}) at 933.9 and 954.1 eV are attributed to the $\text{Cu} 2p_{3/2}$ and $\text{Cu} 2p_{1/2}$, respectively. It is noteworthy that the XPS spectrum is almost unchanged after photocatalytic reaction. This is because the reduced copper species during photocatalytic process can be easily re-oxidized by oxygen when exposed to air after irradiation, which is in good agreement with the previous report [44,61]. This result is also consistent with the XRD analysis of sample C50 before and after irradiation. To prove the existence of Cu^+/Cu^0 during reaction, the cyclic voltammetric behavior of the sample C0.5 was measured and shown in Fig. S1. The redox peaks are observed for the sample, indicating that the various valence of copper in the sample C0.5 during the CV test. As the initial scan polarity is negative, the Cu^{2+} was firstly reduced into Cu^+ , and then further reduced into Cu^0 . And the two oxidation peaks occurred in the positive scan are related to the oxidation from Cu^0 to Cu^+ and finally to Cu^{2+} .

3.6. Transient photocurrent response and EIS analysis

It has been well demonstrated that the separation and transfer efficiency of charge carriers within a photocatalyst is crucial to determine its photocatalytic activity. As such, the transient photocurrent response and the electrochemical impedance spectroscopy were applied to investigate the charge separation behavior of the different samples. Fig. 6a illustrates the comparison of I–t curves of the C0, C0.5 and C4 samples with several on–off cycles of intermittent UV-irradiation. An anodic photocurrent spike is observed in the photocurrent curves of the samples at

the initial time of irradiation, which is caused by the separation of electron–hole pairs at the interface of TiO_2 /electrolyte [62]. Obviously, the highest transient photocurrent was obtained for the C0.5 sample, as compared to the C0 and C4 samples. This is because the small amount of $\text{Cu}_2(\text{OH})_2\text{CO}_3$ loaded onto the surface of TiO_2 can capture the photogenerated electrons from the conduction band of TiO_2 , thus reducing the recombination of photogenerated electrons and holes. However, excess $\text{Cu}_2(\text{OH})_2\text{CO}_3$ in sample C4 functions as recombination centers of photogenerated electrons and holes and leads to a decrease of photocurrent [63].

Further observation indicates that the photocurrent responses of the $\text{Cu}_2(\text{OH})_2\text{CO}_3/\text{TiO}_2$ samples (C0.5 and C4) show different characteristics from that of the pure TiO_2 (C0). Upon turning off the light, the photocurrents of the samples decrease to zero rapidly. After that, the photocurrent intensities of the samples C0.5 and C4 gradually increase even without irradiation, while the photocurrent intensity of the sample C0 remains zero. Combined with the XPS results (Fig. 5) and the XRD patterns (Fig. 1b) of the $\text{Cu}_2(\text{OH})_2\text{CO}_3/\text{TiO}_2$ photocatalysts before and after photocatalytic reaction, it can be deduced that the re-oxidized process of Cu^+/Cu^0 releases electrons and induces the gradually increased photocurrent of the $\text{Cu}_2(\text{OH})_2\text{CO}_3/\text{TiO}_2$ samples in the absence of light irradiation. To weaken the effect of the bias (0.5 V) on the re-oxidized process of Cu^+/Cu^0 , the comparison experiment was conducted at the open circuit voltage (vs. AgCl) for sample C0.5. An analogous photocurrent response was observed, as shown in Fig. 6b.

The charge transfer capability was further investigated by EIS. The radius of the arc on the EIS Nyquist plot reflects the charge transfer kinetics during the photocatalytic process [47]. Normally, smaller semicircle radius of the Nyquist plot implies lower charge transfer resistance, and thus higher separation and transfer rate of electron–hole pairs [64,65]. As can be seen from Fig. 6c, the semicircle radius of the samples increases by the order of C0.5, C0 and C4. In other words, the sample C0.5 experiences a faster charge separation and transfer as compared to C0, while the charge separation and transfer of the sample C4 is suppressed by the excess $\text{Cu}_2(\text{OH})_2\text{CO}_3$. This result is consistent with the transient photocurrent responses and confirms C0.5 as the optimal sample for photocatalytic hydrogen evolution.

3.7. Photocatalytic H_2 -production activity

Photocatalytic H_2 -production activity of the prepared samples was evaluated under the irradiation of a 300 W Xenon lamp using methanol as the sacrificial reagent. No appreciable H_2 production was detected in the absence of either irradiation or photocatalyst. Fig. 7a presents the comparison of the photocatalytic H_2 -production activity of the samples with different $\text{Cu}_2(\text{OH})_2\text{CO}_3$ contents. Pure TiO_2 (C0) shows a very weak photocatalytic activity due to the rapid recombination of electrons and holes. Note that in the presence of even a small amount of $\text{Cu}_2(\text{OH})_2\text{CO}_3$ clusters, the activity of the sample C0.1 is remarkably enhanced. With optimal $\text{Cu}_2(\text{OH})_2\text{CO}_3$ content of 0.5 mol%, the sample C0.5 reached the highest photocatalytic activity of $6713 \mu\text{mol h}^{-1} \text{g}^{-1}$, corresponding to apparent quantum efficiency of 15.4% at 365 nm. Further increasing the $\text{Cu}_2(\text{OH})_2\text{CO}_3$ content leads to a decrease of the photocatalytic activity, which is because the excess $\text{Cu}_2(\text{OH})_2\text{CO}_3$ clusters shield TiO_2 from light harvesting and also act as the recombination centers of photogenerated electrons and holes. It is noteworthy that the photocatalytic H_2 -production activity of sample C0.5 is comparable to that of 0.5 mol% Pt deposited TiO_2 ($6530 \mu\text{mol h}^{-1} \text{g}^{-1}$), suggesting the excellent co-catalytic performance of $\text{Cu}_2(\text{OH})_2\text{CO}_3$ clusters.

Fig. 7b depicts the photocatalytic H_2 -production activity of different Cu specie-containing photocatalysts. It is noteworthy

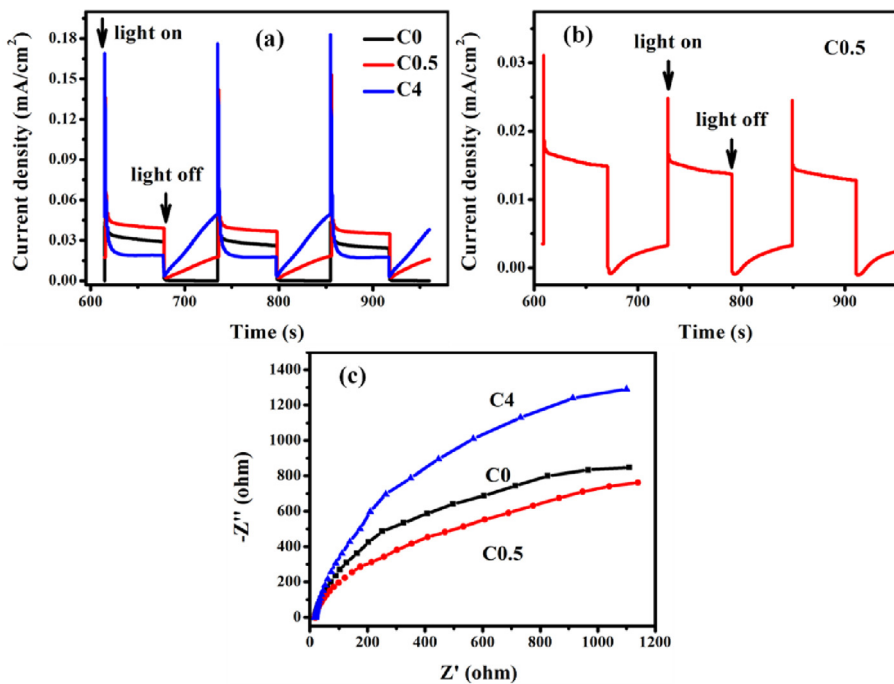


Fig. 6. (a) Transient photocurrent responses of the C0, C0.5 and C4 samples, (b) Transient photocurrent responses of the C0.5 sample at the open circuit voltage (vs. AgCl), and (c) Electrochemical impedance spectra (EIS) of C0, C0.5 and C4 samples.

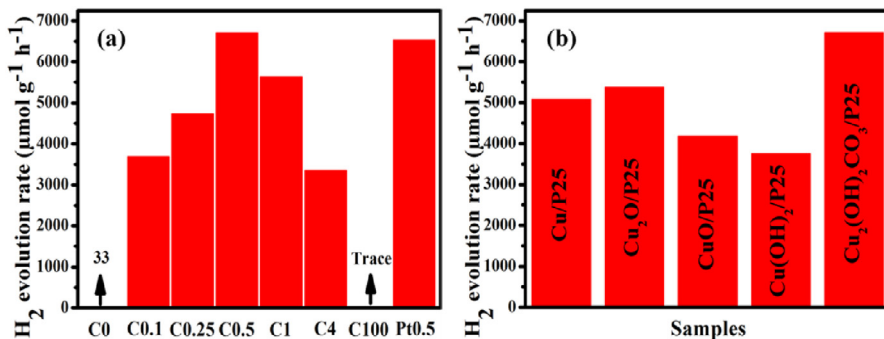


Fig. 7. Comparison of the photocatalytic hydrogen production activity of (a) the samples with different R and Pt/P25; (b) different Cu specie-containing photocatalysts.

that the Cu₂(OH)₂CO₃ modified TiO₂ exhibits the best activity as compared to other copper species modified TiO₂, demonstrating that Cu₂(OH)₂CO₃ clusters are more efficient than other copper species to co-catalyze the photocatalytic hydrogen evolution reaction over TiO₂ photocatalyst. Cu₂(OH)₂CO₃ is a compound based on insoluble Cu(OH)₂ and CuCO₃, whose solubility product constants are 2.2×10^{-20} and 1.4×10^{-10} , respectively. This suggests that Cu₂(OH)₂CO₃ possesses a larger solubility product constant than other Cu-containing species, and thus can release more free Cu²⁺ in aqueous solution. As a result, more Cu⁺/Cu⁰ can be obtained from the photo-reduction of free Cu²⁺, which is responsible for the excellent photocatalytic hydrogen generation [48]. The photocatalytic hydrogen production activities of the sample C0.5 were also evaluated in different pH values (Fig. S2) and temperatures (Fig. S3). It can be found that the photocatalytic hydrogen production activities in acid and basic environment decreased to some extent but are still good. Such decrease can be ascribed to the corrosion of Cu₂(OH)₂CO₃ in acid solution and the consumption of H⁺ in basic solution, respectively. On the other hand, when the temperature of the reaction system is increased to 70 °C, the photocatalytic hydrogen production activity of the sample C0.5 is enhanced as compared to that in ambient condition (actual reaction tempera-

ture of 40 °C). This is due to the thermal effect which could boost the surface catalytic reactions. These results further confirm the excellent co-catalytic performance of Cu₂(OH)₂CO₃ clusters in various conditions.

Cyclic H₂-evolution and long-term H₂-evolution experiments were further carried out to investigate the stability of the Cu₂(OH)₂CO₃/TiO₂ photocatalyst. As shown in Fig. 8a, no obvious loss of activity was observed for the sample C0.5 after cycling test. Moreover, Fig. 8b shows that the sample exhibits a good stability for photocatalytic hydrogen production upon continuous irradiation of 14 h. The results indicate the high stability of the composite photocatalyst for hydrogen production. As demonstrated by the afore-mentioned XRD and XPS results, the copper species remains in the Cu₂(OH)₂CO₃/TiO₂ photocatalysts after photocatalytic reactions. This is because a cyclic redox process among Cu²⁺/Cu⁺/Cu⁰ can occur by repeatedly applying and cutting off light irradiation, which is confirmed by the photoelectrochemical analysis. Moreover, the ultra-small Cu₂(OH)₂CO₃ clusters can be confined in the mesopores of TiO₂, preventing from aggregation and collapse. Therefore, profiting from the recovery process of copper species and structure confinement of the clusters, a high stability of the Cu₂(OH)₂CO₃/TiO₂ photocatalyst is achieved.

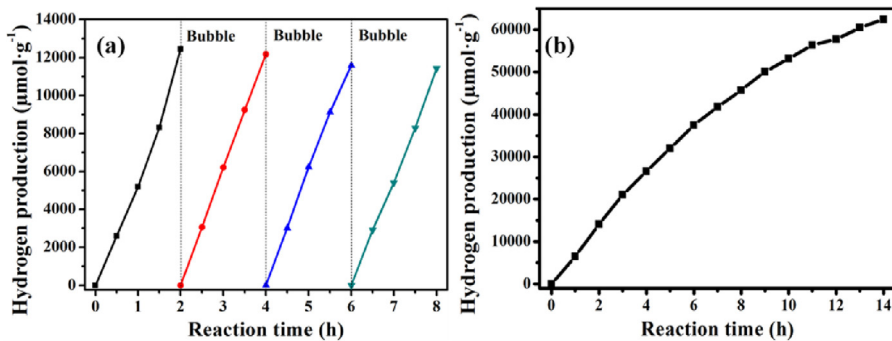


Fig. 8. (a) Cycling runs for the photocatalytic hydrogen evolution in the presence of the C0.5 sample. Every two hours the reaction system is bubbled with N_2 for 30 min to remove the H_2 inside; (b) long-term photocatalytic hydrogen evolution activity in the presence of the C0.5 sample.

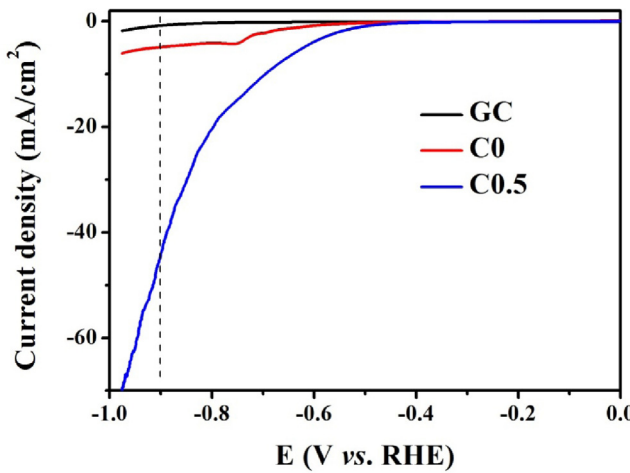


Fig. 9. LSVs for bare GC, samples TiO_2 (C0) and $\text{Cu}_2(\text{OH})_2\text{CO}_3/\text{TiO}_2$ (C0.5) without the light irradiation.

To confirm the role of $\text{Cu}_2(\text{OH})_2\text{CO}_3$ clusters, linear scan voltammograms were recorded for the samples TiO_2 (C0) and $\text{Cu}_2(\text{OH})_2\text{CO}_3/\text{TiO}_2$ (C0.5), as shown in Fig. 9. In comparison with TiO_2 (C0) electrode, $\text{Cu}_2(\text{OH})_2\text{CO}_3/\text{TiO}_2$ exhibits an enhanced current, showing that $\text{Cu}_2(\text{OH})_2\text{CO}_3$ employed here functions as a cocatalyst, promoting the reduction of H^+ to H_2 [66,67]. Combined with the afore-discussed PL results, it can be concluded that the presence of $\text{Cu}_2(\text{OH})_2\text{CO}_3$ facilitates the transfer of the photogenerated electrons from TiO_2 to $\text{Cu}_2(\text{OH})_2\text{CO}_3$, and H^+ can be efficiently reduced by the electrons to generate H_2 , resulting in the enhanced photocatalytic hydrogen production over $\text{Cu}_2(\text{OH})_2\text{CO}_3/\text{TiO}_2$.

A possible photocatalytic mechanism is thus proposed, as illustrated in Fig. 10. Upon light irradiation, a portion of electrons in the VB of TiO_2 are excited into the CB of TiO_2 , and subsequently transfer to $\text{Cu}_2(\text{OH})_2\text{CO}_3$. On the other hand, partial excited electrons directly transfer from the VB of TiO_2 to Cu^{2+} through the direct interfacial charge transfer (IFCT) route [38]. Part of $\text{Cu}_2(\text{OH})_2\text{CO}_3$ is then reduced to Cu^+/Cu^0 . The as-formed Cu^0 species can work as a co-catalyst to reduce the over-potential of water reduction and promote the transfer of photogenerated electrons from the CB of TiO_2 to the tentative $\text{Cu}_2(\text{OH})_2\text{CO}_3/\text{Cu}^+/\text{Cu}^0$ clusters, thus enhancing the photocatalytic H_2 -production activity. After photocatalytic reaction, the Cu^+/Cu^0 can be easily re-oxidized to $\text{Cu}_2(\text{OH})_2\text{CO}_3$, ensuring a good stability and sustainability of the $\text{Cu}_2(\text{OH})_2\text{CO}_3/\text{TiO}_2$ photocatalysts.

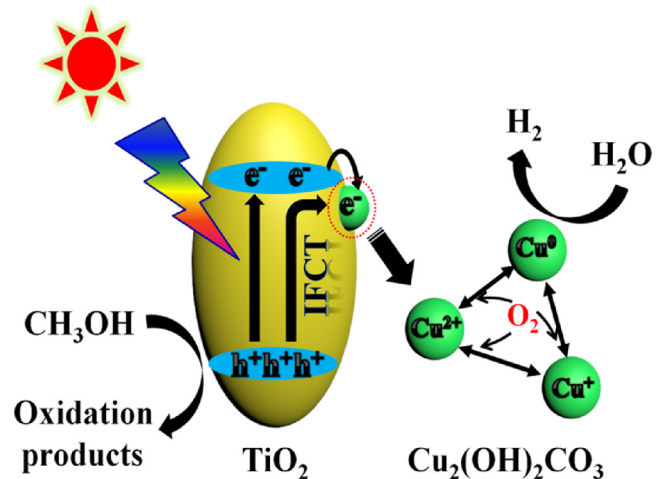


Fig. 10. Schematic illustration for the photocatalytic mechanism of $\text{Cu}_2(\text{OH})_2\text{CO}_3/\text{TiO}_2$ photocatalysts.

4. Conclusions

In summary, $\text{Cu}_2(\text{OH})_2\text{CO}_3$ clusters are successfully incorporated onto the surface of TiO_2 photocatalyst *via* a facile precipitation method. The $\text{Cu}_2(\text{OH})_2\text{CO}_3$ clusters with a small amount act as efficient and stable cocatalysts to enhance the photocatalytic H_2 -production activity of TiO_2 photocatalyst. At an optimal $\text{Cu}_2(\text{OH})_2\text{CO}_3$ content of 0.5 mol%, the $\text{Cu}_2(\text{OH})_2\text{CO}_3/\text{TiO}_2$ photocatalyst exhibits the highest H_2 -production activity of $6713 \mu\text{mol h}^{-1} \text{g}^{-1}$ with the corresponding apparent quantum efficiency of 15.4% at 365 nm, which is comparable to the widely accepted Pt/TiO_2 photocatalyst. The $\text{Cu}_2(\text{OH})_2\text{CO}_3$ clusters are also demonstrated to be more efficient than other copper species, as a substitute for noble metal cocatalyst in the photocatalytic hydrogen evolution reaction. Such enhanced photocatalytic H_2 -production activity is attributed to the formation of $\text{Cu}_2(\text{OH})_2\text{CO}_3/\text{Cu}^+/\text{Cu}^0$ clusters during reaction, which essentially reduce the over-potential of water reduction and promote the transfer of photogenerated electrons from the CB of TiO_2 to the tentative $\text{Cu}_2(\text{OH})_2\text{CO}_3/\text{Cu}^+/\text{Cu}^0$ clusters. Moreover, a high stability of the $\text{Cu}_2(\text{OH})_2\text{CO}_3/\text{TiO}_2$ photocatalyst is promised by the re-oxidation of Cu^+/Cu^0 to $\text{Cu}_2(\text{OH})_2\text{CO}_3$ and structure confinement of $\text{Cu}_2(\text{OH})_2\text{CO}_3$ clusters in the mesopores of TiO_2 . This work provides a protocol of designing highly efficient, stable and low-cost noble-metal-free photocatalytic system for solar-to-fuel conversion.

Acknowledgements

This study was partially supported by the 973 program (2013CB632402), NSFC (51272199, 51320105001, 51372190, 21433007 and 51472191). Also, this work was financially supported by the Natural Science Foundation of Hubei Province of China (2015CFA001), the Fundamental Research Funds for the Central Universities (WUT: 2015-III-034) and Innovative Research Funds of SKLWUT (2015-ZD-1).

Appendix A. Supplementary data

Supplementary data associated with this article can be found, in the online version, at <http://dx.doi.org/10.1016/j.apcatb.2016.12.031>.

References

- [1] P. Zhou, J. Yu, M. Jaroniec, *Adv. Mater.* 26 (2014) 4920–4935.
- [2] P. Zhang, T. Wang, H. Zeng, *Appl. Surf. Sci.* 391 (2016) 404–414.
- [3] J.H. Yang, D.G. Wang, H.X. Han, C. Li, *Acc. Chem. Res.* 46 (2013) 1900–1909.
- [4] V. Preethi, S. Kanmani, *Mater. Sci. Semicond. Process.* 16 (2013) 561–575.
- [5] A.B. Djurišić, Y.H. Leung, A.M.C. Ng, *Mater. Horiz.* 1 (2014) 400–410.
- [6] T. Hisatomi, J. Kubota, K. Domen, *Chem. Soc. Rev.* 43 (2014) 7520–7535.
- [7] Q. Xiang, B. Cheng, J. Yu, *Angew. Chem., Int. Ed.* 54 (2015) 11350–11366.
- [8] A. Fujishima, K. Honda, *Nature* 238 (1972) 37–38.
- [9] S. Cao, J. Yu, *Photochem. Photobiol. C* 27 (2016) 72–99.
- [10] Y. Xu, R. Xu, *Appl. Surf. Sci.* 351 (2015) 779–793.
- [11] L. Liu, Y. Qi, J. Hu, Y. Liang, W. Cui, *Appl. Surf. Sci.* 351 (2015) 1146–1154.
- [12] C.P. Sajan, S. Waghé, A.A. Al-Ghamdi, J. Yu, S. Cao, *Nano Res.* 9 (2016) 3–27.
- [13] Q.J. Xiang, J.G. Yu, *J. Phys. Chem. Lett.* 4 (2013) 753–759.
- [14] R. Michal, E. Dwornicze, M. Caplovicova, O. Monfort, P. Lianos, L. Caplovic, G. Plesch, *Appl. Surf. Sci.* 371 (2016) 538–546.
- [15] S. Hu, F. Zhou, L. Wang, J. Zhang, *Catal. Commun.* 12 (2011) 794–797.
- [16] J. Low, B. Cheng, J. Yu, *Appl. Surf. Sci.* 392 (2017) 658–686.
- [17] J. Wen, X. Li, W. Liu, Y. Fang, J. Xie, Y. Xu, *Chin. J. Catal.* 36 (2015) 2049–2070.
- [18] Y. Li, W. Zhang, X. Shen, P. Peng, L. Xiong, Y. Yu, *Chin. J. Catal.* 36 (2015) 2229–2236.
- [19] J. Fu, S. Cao, J. Yu, J. Low, Y. Lei, *Dalton Trans.* 43 (2014) 9158–9165.
- [20] Y. Wang, J. Yu, W. Xiao, Q. Li, *J. Mater. Chem. A* 2 (2014) 3847–3855.
- [21] M. Wang, M. Ye, J. Iocozzia, C. Lin, Z. Lin, *Adv. Sci.* 3 (2016) 1600024.
- [22] H. Park, H. Kim, G. Moon, W. Choi, *Energy Environ. Sci.* 9 (2016) 411–433.
- [23] J. Shi, X. Guan, Z. Zhou, H. Liu, L. Guo, J. Nanopart. Res. 17 (2015) 252–264.
- [24] R. Jaiswal, J. Bharambe, N. Patel, A. Dashora, D.C. Kothari, A. Miotello, *Appl. Catal. B* 168–169 (2015) 333–341.
- [25] L. Kernazhitsky, V. Shymanova, T. Gavrilko, V. Naumov, V. Kshnyakin, T. Khalyavka, *J. Solid State Chem.* 198 (2013) 511–519.
- [26] M.Z. Lin, H. Chen, W.F. Chen, A. Nakaruk, P. Koshy, C.C. Sorrell, *Int. J. Hydrogen Energy* 39 (2014) 21500–21511.
- [27] S. Ivanov, A. Barylak, K. Besaha, A. Bund, Y. Bobitski, R. Wojnarowska-Nowak, I. Yaremchuk, M. Kus-Liskiewicz, *Nanoscale Res. Lett.* 11 (2016) 140–152.
- [28] X.F. Lei, X.X. Xue, H. Yang, C. Chen, X. Li, M.C. Niu, X.Y. Gao, Y.T. Yang, *Appl. Surf. Sci.* 332 (2015) 172–180.
- [29] X. Li, J. Yu, J. Low, Y. Fang, J. Xiao, X. Chen, *J. Mater. Chem. A* 3 (2015) 2485–2534.
- [30] M.R. Gholipour, C.T. Dinh, F. Beland, T.O. Do, *Nanoscale* 7 (2015) 8187–8208.
- [31] J. Xing, J.F. Chen, Y.H. Li, W.T. Yuan, Y. Zhou, L.R. Zheng, H.F. Wang, P. Hu, Y. Wang, H.J. Zhao, Y. Wang, H.G. Yang, *Chem. Eur. J.* 20 (2014) 2138–2144.
- [32] Y. Xu, C. Zhang, L. Zhang, X. Zhang, H. Yao, J. Shi, *Energy Environ. Sci.* 9 (2016) 2410–2417.
- [33] B. Gupta, A.A. Melvin, T. Matthews, S. Dash, A.K. Tyagi, *Renew. Sustain. Energy Rev.* 58 (2016) 1366–1375.
- [34] E.P. Melián, C.R. López, D.E. Santiago, R. Quesada-Cabrera, J.A.O. Méndez, J.M.D. Rodríguez, O.G. Díaz, *Appl. Catal. A* 518 (2016) 189–197.
- [35] A. Meng, J. Zhang, D. Xu, B. Cheng, J. Yu, *Appl. Catal. B* 198 (2016) 286–294.
- [36] Y. Choi, H. Kim, G. Moon, S. Jo, W. Choi, *ACS Catal.* 6 (2016) 821–828.
- [37] Y. Liu, Z. Wang, W. Huang, *Appl. Surf. Sci.* 389 (2016) 760–767.
- [38] S. Obregón, M.J. Muñoz-Batista, M. Fernández-García, A. Kubacka, G. Colón, *Appl. Catal. B* 179 (2015) 468–478.
- [39] M.K. Kumar, K. Bhavani, G. Naresh, B. Srinivas, A. Venugopal, *Appl. Catal. B* 199 (2016) 282–291.
- [40] A. Kubacka, M.J. Muñoz-Batista, M. Fernández-García, S. Obregón, G. Colón, *Appl. Catal. B* 163 (2015) 214–222.
- [41] S. Zhang, H. Wang, M. Yeung, Y. Fang, H. Yu, F. Peng, *Int. J. Hydrogen Energy* 38 (2013) 7241–7245.
- [42] W.J. Foo, C. Zhang, G.W. Ho, *Nanoscale* 5 (2013) 759–764.
- [43] I. Mondal, U. Pal, *Phys. Chem. Chem. Phys.* 18 (2016) 4780–4788.
- [44] M. Lei, N. Wang, L.H. Zhu, Q.L. Zhou, G. Nie, H.Q. Tang, *Appl. Catal. B* 182 (2016) 414–423.
- [45] Z. Xi, C. Li, L. Zhang, M. Xing, J. Zhang, *Int. J. Hydrogen Energy* 39 (2014) 6345–6353.
- [46] Y. Li, B. Wang, S. Liu, X. Duan, Z. Hu, *Appl. Surf. Sci.* 324 (2015) 736–744.
- [47] S. Xiao, P. Liu, W. Zhu, G. Li, D. Zhang, H. Li, *Nano Lett.* 15 (2015) 4853–4858.
- [48] Q. Hu, J. Huang, G. Li, Y. Jiang, H. Lan, W. Guo, Y. Cao, *Appl. Surf. Sci.* 382 (2016) 170–177.
- [49] J. Yu, J. Ran, *Energy Environ. Sci.* 4 (2011) 1364–1371.
- [50] S.S. Lee, H. Bai, Z. Liu, D.D. Sun, *Environ. Sci. Technol.* 49 (2015) 2541–2548.
- [51] X. An, H. Liu, J. Qu, S.J.A. Moniz, J. Tang, *New J. Chem.* 39 (2015) 314–320.
- [52] H. Eskandarloo, A. Badiei, M.A. Behnajady, G.M. Ziarani, *Photochem. Photobiol.* 91 (2015) 797–806.
- [53] W. Zhang, Y. Liu, B. Yu, J. Zhang, W. Liang, *Mater. Sci. Semicond. Process.* 30 (2015) 527–534.
- [54] A. Petala, E. Ioannidou, A. Georgaka, K. Bourikas, D.I. Kondarides, *Appl. Catal. B* 178 (2015) 201–209.
- [55] M. Liu, X.Q. Qiu, M. Miyauchi, K. Hashimoto, *Chem. Mater.* 23 (2011) 5282–5286.
- [56] M. Thommes, K. Kaneko, A.V. Neimark, J.P. Olivier, F. Rodriguez-Reinoso, J. Rouquerol, K.S.W. Sing, *Pure Appl. Chem.* 87 (2015) 1051–1069.
- [57] E.P. Melian, O.G. Diaz, A.O. Mendez, C.R. Lopez, M.N. Suarez, J.M.D. Rodriguez, J.A. Navio, D.F. Hevia, J.P. Pena, *Int. J. Hydrogen Energy* 38 (2013) 2144–2155.
- [58] H. Dang, X. Dong, Y. Dong, Y. Zhang, S. Hampshire, *Int. J. Hydrogen Energy* 38 (2013) 2126–2135.
- [59] H. Dang, X. Dong, Y. Dong, H. Fan, Y. Qiu, *Mater. Lett.* 138 (2015) 56–59.
- [60] Z. Jin, W. Duan, B. Liu, X. Chen, F. Yang, J. Guo, *Appl. Surf. Sci.* 356 (2015) 707–718.
- [61] X. Liu, L. Cao, W. Sun, Z. Zhou, J. Yang, *Res. Chem. Intermed.* 42 (2016) 6289–6300.
- [62] Q. Xiang, J. Yu, M. Jaroniec, *Nanoscale* 3 (2011) 3670–3678.
- [63] L. Li, B. Cheng, Y. Wang, J. Yu, *J. Colloids Interface Sci.* 449 (2015) 115–121.
- [64] W. Chen, T.Y. Liu, T. Huang, X.H. Liu, G.R. Duan, X.J. Yang, S.M. Chen, *RSC Adv.* 5 (2015) 101214–101220.
- [65] J.R. Ran, J. Zhang, J.G. Yu, S.Z. Qiao, *ChemSusChem* 7 (2014) 3426–3434.
- [66] Y. Wang, S. Ma, Q. Li, Y. Zhang, X. Wang, X. Han, *ACS Sustain. Chem. Eng.* 4 (2016) 3773–3779.
- [67] Y. Zhao, Z. Yang, Y. Zhang, L. Jing, X. Guo, Z. Ke, P. Hu, G. Wang, Y. Yan, K. Sun, *J. Phys. Chem. C* 118 (2014) 14238–14245.